Evolution of Magnetism in Magnetic Topological Semimetal $NdSb_xTe_{2-x+\delta}$

Santosh Karki Chhetri[1], Rabindra Basnet[1,2#], Jian Wang[4], Krishna Pandey[3], Gokul Acharya[1], Md Rafique Un Nabi[1], Dinesh Upreti[1], Josh Sakon[5], Mansour Mortazavi[2], Jin Hu[1,3*]

[1]Department of Physics, University of Arkansas, Fayetteville, AR 72701, USA

[2]Department of Chemistry & Physics, University of Arkansas at Pine Bluff, Pine Bluff, Arkansas 71603, USA

[3]Materials Science and Engineering Program, Institute for Nanoscience and Engineering, University of Arkansas, Fayetteville, AR 72701, USA

[4]Department of Chemistry and Biochemistry, Wichita State University, Wichita, KS 67260, USA

[5]Department of Chemistry & Biochemistry, University of Arkansas, Fayetteville, AR 72701, USA

Abstract

Magnetic topological semimetals *Ln*SbTe (*Ln* = Lanthanide) have attracted intensive attention because of the presence of interplay between magnetism, topological, and electron correlations depending on the choices of magnetic *Ln* elements. Recently, varying Sb-Te composition has been found to effectively control the electronic and magnetic states in $LnSb_xTe_{2-x}$. With this motivation, we report the evolution of magnetic properties with Sb-Te substitution in $NdSb_xTe_{2-x+\delta}$, ($0 \leq x \leq 1$). Our work reveals the interesting non-monotonic change in magnetic ordering temperature with varying composition stoichiometry. In addition, reducing the Sb content *x* drives the reorientation of moments from in-plane (*ab*-plane) to out-of-plane (*c*-axis) direction that results in the distinct magnetic structures for two end compounds $NdTe_2$ ($x = 0$) and NdSbTe ($x = 1$). Furthermore, the moment orientation in $NdSb_xTe_{2-x+\delta}$ is also found to be strongly tunable upon application of weak magnetic field, leading to rich magnetic phases depending on the composition stoichiometry, temperature, and magnetic field. Such strong tuning of magnetism in this material establishes it as a promising platform for investigating tunable topological states and correlated topological physics.

basnetr@uapb.edu

jinhu@uark.edu

I. Introduction

Topological semimetals (TSMs) such as Dirac or Weyl semimetals feature symmetry-protected linearly dispersed Dirac or Weyl cones in their electronic structures, which host relativistic fermions with low-energy excitations can be described by Dirac or Weyl equations respectively [1,2]. In contrast to Dirac or Weyl nodes at discrete points in the momentum space in Dirac and Weyl semimetals, another class of TSMs i.e., nodal-line semimetals exhibit interesting linear band crossings along one-dimensional loops or lines. Various exotic properties have been discovered, such as large magnetoresistance [3], ultrahigh mobility [3], chiral anomaly [4,5], and surface Fermi arcs [6–9], providing deeper understanding of fundamental topological physics as well as opportunities for future technological applications. Within these categories of TSMs, there has recently been rapidly growing interest in magnetic TSMs such as $Co_2Mn(Al/Ga)$ [10–14], $Co_3Sn_2S_2$ [15,16], FeSn [17], Fe_3Sn_2 [18], $Fe_3(Al/Ga)$ [19], Fe_3GeTe_2 [20], $Mn_3(Ge/Sn)$ [21–24], and GdPtBi [25]. These compounds offer a rare platform to investigate interplay between magnetism and non-trivial band topology, which can generate novel exotic quantum phenomena such as large intrinsic anomalous Hall effect [26] and anomalous Nernst effect [27].

As described above, the magnetism in the majority of magnetic TSMs reported so far originates from 3*d* transition metal elements. In addition to transition metal-based compounds, magnetic lanthanide (*Ln*)-based TSMs are also highly desired because of strong correlation effects brought by the 4*f* electrons. The *Ln*SbTe compounds represent one such model example [28–44]. *Ln*SbTe belongs to ZrSiS-type nodal-line semimetal family that can be represented by a general chemical formula *WHM* (*W*= Zr/Hf/lanthanides; *H*=Si/Ge/Sn/Sb, *M* = S, Se,Te). Those materials crystallize in a layered PbFCl-type crystal structure (space group *P*4/*nmm*), characterized by square or nearly square net layers of *H*-atoms which harbor relativistic fermions [28,31,45–60]. In

*Ln*SbTe, the presence of magnetic *Ln* element such as Ce [28–30], Nd [37,38,44], Sm [35,36], Gd [31–33], Tb [42,43], Dy [41,44], Ho [39,40,43], and Er [44] activates the spin degree of freedom that leads to diverse antiferromagnetic (AFM) ground states depending on the choice of *Ln* [28,31,35,37,39,41,44]. Varying *Ln* element is also found to tune the topological states generated by Sb layers [28,31,35,39–41,57,58,61,62], providing opportunity to engineer band topology via coupling between magnetism and electronic bands [28]. Furthermore, rich quantum phenomena such as Kondo effect, charge density waves (CDWs), and correlation enhancement have been reported in various *Ln*SbTe compounds [28,29,33,35,37,61,63,64], which are also strongly dependent on the choices of *Ln* elements.

Besides magnetism from *Ln*, tuning Sb-Te composition stoichiometry has been established as an effective approach to engineer electronic and magnetic phases in $LnSb_xTe_{2-x}$ [33,36,61,62,62,62,63,65]. Given that the square-net lattices are inherently unstable [66], doping electrons by substituting Te for Sb causes distortion of Sb-square net and the subsequent formation of CDWs, which has been found to modify electronic band structures and intrinsic magnetism [33,36,61–63,65]. In $LnSb_xTe_{2-x}$, the magnetism has been found to be effectively tunable with varying Sb composition *x*, however the Sb-Te substitution induces distinct evolution of magnetic properties in few *Ln*SbTe (*Ln* = Ce [30], Sm [36], and Gd [33,63]) compounds despite of similar crystal symmetry and structure evolution from tetragonal (space group *P*4/*nmm*) to orthorhombic (space group *Pmmm*) phase in off-stoichiometric compositions. While numerous stoichiometric *Ln*SbTe compounds [28,29,33,35,37,61,63,64] have been discovered, the evolution of magnetism by tuning composition in off-stoichiometric compounds is still in an early stage. Only recently, a neutron diffraction study has determined the modification of magnetic structure with varying Sb-Te composition in $NdSb_{0.94}Te_{0.92}$ and $NdSb_{0.48}Te_{1.37}$ [65]. Such promising results

demand a complete understanding of magnetism and possible tuning of topological states over entire Sb-Te composition in $NdSb_xTe_{2-x}$. In this work, we present the evolution of magnetic properties from $x = 0$ to 1 in $NdSb_xTe_{2-x}$. Our work reveals an interesting non-monotonic variation of magnetic ordering temperature (T_N) and the reorientation of Nd moments with Sb-Te substitution. These results provide a rich platform for tunable topological states and further studying the correlated topological physics.

II. Experiment

The $NdSb_xTe_{2-x+\delta}$ ($0 \leq x \leq 1$, δ represents possible vacancies) single crystals used in this work were synthesized by a chemical vapor transport (CVT) method using I_2 as the transport agent. The pristine $NdTe_2$ was grown by a direct CVT method with elementary Nd and Te powders as source materials. For each of the other compositions with Sb, a polycrystalline precursor is necessary to minimize vacancies (as discussed below). Each precursor was prepared by heating the mixture of Nd with different ratios of Sb and Te powders (shown in Table I) at 850 °C for 2 days. The single crystals were obtained via CVT with a temperature gradient from 1000 to 850 °C for two weeks. The elemental compositions and crystal structures of the obtained crystals were examined by energy-dispersive x-ray spectroscopy (EDS) and x-ray diffraction (XRD), respectively. Magnetization measurements up to 9 T were performed by using a physical property measurement system (PPMS, Quantum Design). Magnetization measurements up to 7 T and angular dependent magnetization were performed by using a magnetic property measurement system (MPMS, Quantum Design) equipped with a rotator.

III. Result and discussion

Recent surge of interests in TSMs featuring a square net of atoms has motivated the study of *Ln*SbTe family [28–44]. While the square net planes in majority of *WHM* compounds are formed by group-IV elements *H* = Si, Ge, and Sn [45–56,67], a Sb (group-V) square net sandwiched by *Ln*-Te bilayers is present in *Ln*SbTe compounds. Previous studies have demonstrated that the synthesis of ideal stoichiometric *Ln*SbTe compounds is challenging [29,37,65] and often yield various off-stoichiometric $LnSb_xTe_{2-x}$ ($0 < x < 1$) compositions consisting of distorted Sb plane [33,36,61,62,62,62,63,65]. Such off-stoichiometry is also accompanied by vacancies in the Sb [33,36,63–65] and Te [33,61,62,65] layers that enhance with reducing Sb content [36,63,65], and eventually after complete substitution of Te for Sb produces a strong Te vacancy in structurally similar $LnTe_2$ compounds [68,69]. The chalcogen vacancy widely occurs in LnX_2 (X = S, Se, and Te), which has been ascribed to the presence of mixed anions $(X_2)^{2-}$ and $(X)^{2-}$ in chalcogen layer [69,70] and favored by decreasing Ln^{3+} cation radius along the lanthanide series [70]. Therefore, chalcogen vacancy is usually seen in compounds with smaller Ln^{3+} cations such as $NdTe_{1.89}$ [68], $SmTe_{1.84}$ [71], $GdTe_{1.80}$ [72], $TbTe_{1.80}$ [72], and $DyTe_{1.80}$ [72]. Replacing Sb for Te in these compounds induces hole doping and consequently reduces the number of vacancies required for charge balance in Te layers [63].

In $NdSb_xTe_{2-x}$ studied in this work, both slight [65] and the lack [44] of Te vacancy are observed in a nearly-stoichiometric composition. Although an earlier study on $CeSb_xTe_{2-x-\delta}$ [62] has claimed less effect of Te vacancy on magnetization, we selected $NdSb_xTe_{2-x}$ samples with minimum vacancy to ensure the systematic tuning of magnetization with varying composition and without the interference of vacancy effects. The millimeter-size single crystals in the whole compositional range from $NdTe_2$ ($x = 0$) to $NdSbTe_{1.08}$ ($x = 1$) were obtained using CVT [Fig. 1(a)],

similar to previous NdSbTe growths [37,38,44]. Our EDS results have revealed the nearly 1:2 stoichiometric composition ratio between Nd and (Sb+Te) (Table I), from which we conclude the absence of vacancies within the resolution limit of our instrument. Such observation is in contrast to the reported Ce, Sm, and Gd sibling compounds [33,36,62–64], which might be due to the slight difference in synthesis method and sample screening. However, we observed a slight excess of Te in our composition analysis. Therefore, our samples can be represented as $NdSb_xTe_{2-x+\delta}$, where δ = 0-0.08 denotes the excess Te that might be due to the instrument error or partial accommodation into the Sb layer, as seen in CeSbTe [29] and GdSbTe [63]. As shown in Table I, the nominal composition in source materials is found to yield significantly different composition (determined by EDS) in the grown crystals, consistent with previous Sb-Te substitution studies in this family [36,63]. Earlier work on $GdSb_xTe_{2-x-\delta}$ has adopted an strategy of adding more Sb in the starting materials to obtain crystals with increasing x [63]. In contrast, we did not observe a systematic correlation between nominal and final compositions among the grown crystals [Table I], indicating the difficulty to control composition stoichiometry in $NdSb_xTe_{2-x+\delta}$. This could be the reason for the lack of a complete Sb-Te evolution study for this compound although NdSbTe [37] was one of the earliest studied *Ln*SbTe compounds.

The stoichiometric *Ln*SbTe compounds crystallize in tetragonal (space group *P*4/*nmm*) structure [28–44], which on substituting Te for Sb results in structure transition to orthorhombic phase at around x = 0.7 to 0.85 in $LnSb_xTe_{2-x}$ (*Ln* = Ce [30], Sm [36], and Gd [63]). The structural information determined by our structure refinement using powder XRD spectra presented in Fig. 1(b) also reveals an orthorhombic distortion at around $x \approx 0.70$ in $NdSb_{x-\delta}Te_{2-x+\delta}$ that is accompanied by shrinking *c*-axis and expanding *ab*-plane [Fig. 1(c)], consistent with other $LnSb_xTe_{2-x}$ (*Ln* = Ce, Sm, and Gd) members [36,62,63]. The tetragonal crystal lattice is retained

on further decreasing the Sb content below $x \approx 0.18$ leading to tetragonal structure for $NdTe_2$ ($x = 0$). Both tetragonal and orthorhombic structures have been reported in Te-deficient compounds $NdTe_{1.80}$ [73] and $NdTe_{1.89}$ [68], respectively. The tetragonal structure has been identified in analogous compounds $CeTe_2$ [74] and $PrTe_2$ [75] whereas $LaTe_2$ crystallizes in monoclinic structure [76]. The tetragonal and orthorhombic structures are very similar and could be difficult to distinguish during crystal structure refinement. In addition, because of the presence of CDW in this material family (especially in the Sb-less compositions), the refinement results could be influenced by the additional CDW satellite peaks. Unfortunately, the impact of CDW in the crystal structure refinement for our $NdSb_{x-\delta}Te_{2-x+\delta}$ samples is difficult to clarify due to instrument limitation of our x-ray diffractometer. For this, a synchrotron light source is needed, which could be the scope for future studies that might also clarify the evolution of CDW with composition stoichiometry in $NdSb_xTe_{2-x+\delta}$. Though we are not able to examine CDW due to instrumental limitations, the re-emergence of tetragonal structure for $x < 0.18$ in $NdSb_xTe_{2-x+\delta}$ can be understood by the evolution of XRD spectra with varying composition stoichiometry. As shown in Fig. 1b, the XRD spectra display clear peak splitting for samples with intermediate Sb content (indicated by the red arrows), which is consistent with the lowering symmetry from tetragonal to orthorhombic.

With the orthorhombically distorted lattice, the 2D Sb square net characterized by identical Sb-Sb bonding length and 90° bonding angles in stoichiometric has been found to undergo deviation of bonding angles from 90° with reducing Sb content that indicates the distorted Sb square plane [36,62,63,65]. Distorted Sb-square nets in orthorhombic crystal lattice depending on the composition stoichiometry in *Ln*SbTe are reported to drive tunable CDWs [33,36,61–63,65]. Even the formation of CDW has been revealed in tetragonal $CeTe_2$ [77–79] and $PrTe_2$ [77] as well as monoclinic $LaTe_2$ [80]. The CDW is found to strongly interplay with magnetism in *Ln*SbTe

leading to complex magnetic phases in off-stoichiometric compositions [33,62,65] and even a modification of a collinear AFM structure in a nearly stoichiometric composition to a more complex elliptical cycloid magnetic structure for a Sb-less composition in $NdSb_xTe_{2-x-\delta}$ [65]. To investigate the evolution of magnetic properties over entire composition range in $NdSb_xTe_{2-x+\delta}$, we have measured the temperature dependence of susceptibility $\chi(T)$ under in-plane ($H//ab$) and out-of-plane ($H//c$) magnetic fields of $\mu_0 H = 0.1$ T [Fig. 2(a)] in order to investigate the variation of T_N and moment orientation with Sb-Te substitution. Similar to the previous studies [35,37,41,44,63], T_N for each sample, except for $x = 0.29$, is extracted from the susceptibility peak or anomaly in in-plane ($\chi_{//}$, measured with field parallel to the ab-plane) and out-of-plane ($\chi_{\perp}$; measured with field parallel to the c-axis) susceptibility measurements, as indicated by the solid triangles in Fig. 2a. The obtained transition temperatures are consistent with that determined from the derivative susceptibility $d\chi/dT$ [Fig. 2(b)]. Furthermore, for the $x = 0.29$ sample which does not display clear feature in susceptibility measurement, the derivative susceptibility reveals the possible magnetic transition temperature, as shown in Fig. 2b. The extracted T_N of 2.04 K for the end compounds $NdTe_2$ ($x = 0$) is distinct from the lack of magnetic ordering down to 2 K in $NdTe_{1.89}$ with significant Te vacancy [68]. Such difference might be attributed to the suppression of Te-mediated magnetic interaction between Nd moments. For the other end compound $NdSbTe_{1.08}$ ($x = 1$), $T_N \approx 2.74$ K is consistent with the nearly-stoichiometric composition $NdSb_{0.94}Te_{0.92}$ [65] but slightly lower than the ideal stoichiometry NdSbTe ($T_N \approx 3.1$ K) [44]. In Fig. 3(a) we summarized the magnetic transition temperatures for our samples, which exhibit a non-monotonic composition dependence. Both monotonic [62] and non-monotonic [63] composition-dependent T_N have been observed in $LnSb_xTe_{2-x}$. In $CeSb_xTe_{2-x}$ [62], the T_N systematically increases with decreasing Sb content x, while a similar non-monotonic composition

dependence of T_N is seen in $GdSb_xTe_{2-x}$ [63]. The monotonic variation of T_N in $CeSb_xTe_{2-x}$, which is in contrast to Nd and Gd samples, might be attributed to difference in interplay between CDWs and magnetism [65] arising from the distinct moment orientation in CeSbTe [62] as compared to NdSbTe [65] and GdSbTe [33]. In $LnSb_xTe_{2-x}$, the CDWs exhibit single modulation wave-vector $\boldsymbol{q}$ within the Sb plane in the intermediate Sb-composition range i.e., (0.21-0.34) < x < (0.74-0.85) whereas below x < (0.21-0.34) these compounds host multiple $\boldsymbol{q}$-vectors along different crystallographic axes [62,63]. The out-of-plane moment orientation in $CeSb_xTe_{2-x}$ [62] does not align with CDW $\boldsymbol{q}$-vector, especially in single $\boldsymbol{q}$-vector (aligned along the *ab*-plane) region for intermediate Sb-composition, resulting in relatively weaker interplay between CDW and magnetism, thus causing the systematic variation of T_N. On the other side, the in-plane orientation of moments in NdSbTe [65] and GdSbTe [33] might strongly couple with in-plane CDW $\boldsymbol{q}$-vector leading to non-monotonic dependence of T_N with Sb-Te substitution.

As seen in Fig. 3(a), the non-monotonic composition dependence of T_N in $NdSb_xTe_{2-x+\delta}$ involves three distinct regions featuring different orientations for Nd moments: (1) within *ab*-plane (represented as AFM_{ab}) for Sb-rich compositions, (2) canted configuration (cAFM) for intermediate Sb-compositions, and (3) along *c*-axis (AFM_c) for Sb-less compositions. These moment orientations were determined by $\chi(T)$ and were further confirmed by field dependence of magnetization $M(H)$ measurements shown in Fig. 4. Starting with pristine $NdSbTe_{1.08}$ (x = 1), the $\chi_{//}$ gradually decreases below $T_N \approx 2.74$ K, in contrast to weakly temperature-dependent $\chi_{\perp}$. This is suggestive of an in-plane AFM configuration, consistent with the reported magnetic structure for nearly-stoichiometric $NdSb_{0.94}Te_{0.92}$ [65]. Decreasing Sb content to x = 0.82, similar $\chi(T)$ trend with unchanged T_N (≈ 2.78 K) is observed [Fig. 3(a)], indicating a similar magnetic ordering to that of the x = 1 compound. The in-plane easy axis is also supported by the $M(H)$ measurements

under in-plane ($H//ab$) and out-of-plane ($H//c$) magnetic fields at T = 2 K. As shown in Fig. 4, for both x = 1 and 0.82, the in-plane ($M_{//}$; magnetization parallel to the ab-plane) isothermal magnetization is larger than the out-of-plane ($M_{\perp}$; magnetization parallel to the c-axis) magnetization, which implies that the easy axis should align towards the ab-plane. The magnetic anisotropy in these samples is further manifested in the angular dependence of susceptibility [$\chi(\theta)$] measurements for samples representing three different AFM regions [AFM_{ab}, cAFM, and AFM_c in Fig. 3(a)] at T = 2 K and $\mu_0 H$ = 0.1 T [Fig. 3(c)]. For x = 1, the susceptibility is maximum and minimum along the in-plane and out-of-plane fields respectively, which is in line with $\chi(T)$ and $M(H)$ measurements.

This scenario completely changes after entering into the orthorhombically distorted regime ($x < 0.70$). As shown in Fig. 2(a), in contrast to the Sb rich samples that display strong drop in $\chi_{//}$ while roughly constant $\chi_{\perp}$, both $\chi_{//}$ and $\chi_{\perp}$ exhibit clear peaks in the x = 0.60 sample followed by a sharp drop and then remain relatively flat down to the lowest measured temperature. Such a similar temperature-dependent behavior down to the lowest measured temperature along the both field directions suggests a spiral spin texture with a canted spin component [33]. The moment canting scenario is consistent with the reported elliptical cycloid magnetic structure propagating along the b-axis but also with a non-zero out-of-plane component determined by neutron diffraction experiment for $NdSb_{0.48}Te_{1.48}$ [65]. The elliptical cycloid magnetic structure with both in-plane and out-of-plane moment components can also be understood by relatively less anisotropy between field-dependent $M_{//}$ and $M_{\perp}$ [81] at T = 2 K for x = 0.60 and 0.45 (Fig. 4). Furthermore, the weaker magnetic anisotropy in orthorhombic regime as compared to $x > 0.70$ tetragonal samples is clearly demonstrated by the lack of significant anisotropy in the $\chi(\theta)$ measurement in x = 0.60 [Fig. 3(c)]. Despite the well-defined peaks in both $\chi_{//}$ and $\chi_{\perp}$ for x = 0.60, the drop of $\chi_{//}$ below T_N is more

pronounced than $\chi_{\perp}$, which implies the nearly in-plane orientation for canted moments that agrees well with the higher (about 3 times) in-plane than the out-of-plane component in elliptical cycloid magnetic structure for $NdSb_{0.48}Te_{1.48}$ [65]. The moments remain canted for x = 0.45, as demonstrated by the similar magnetic transitions in both $\chi_{//}$ and $\chi_{\perp}$ at a slightly higher T_N (≈ 2.9 K) but reducing the Sb content from x = 0.60 to 0.45 pushes the moments away from the *ab*-plane because the decrease in $\chi_{//}$ and $\chi_{\perp}$ below T_N is much more comparable that that of x = 0.60. The spin reorientation in the intermediate Sb-regime has been attributed to the interplay between CDW and magnetism [65], which is in line with the fact that both T_N and moment orientation essentially remain unchanged in the tetragonal regime (x > 0.70) where the CDW is absent [62,63]. Such coupling between CDW and magnetism has also been proposed to relieve the magnetic frustration arising due to the competition between nearest-neighbor AFM and ferromagnetic (FM) interactions in a nearly-stoichiometric $NdSb_{0.94}Te_{0.92}$ [65]. In fact, in our x = 1 sample, the PM to AFM transition lacks a sharp peak but is reflected by the broad transition in $\chi_{//}$, indicating frustrated magnetic ordering consistent with a similar composition $NdSb_{0.94}Te_{0.92}$ [65]. The broad T_N peak in x = 1 starts to become sharper with decreasing x leading to sharp magnetic transitions in x = 0.60 and 0.45, suggesting the suppression of frustration when CDW is functional. Furthermore, relieving the magnetic frustration would strengthen the magnetic interactions, which explains the systematic rise of T_N with reducing Sb content from x = 1 until reaching a maximum value for x = 0.45 [Fig. 3(a)]. The maximal T_N around x = 0.45 is also seen in $GdSb_xTe_{2-x-\delta}$ [63], suggesting a similar scenario of coupling between CDW and in-plane magnetic moments in GdSbTe [33].

The T_N reduces on further decreasing the Sb content from x = 0.45 to 0.29. The drop of T_N for x = 0.29 nearly coincides with the phase boundary between single and multiple CDW $\boldsymbol{q}$-vectors identified in $CeSb_xTe_{2-x-\delta}$ [62] and $GdSb_xTe_{2-x-\delta}$ [63], therefore further decreasing the Sb content

modifies the CDW which is expected to tune the magnetic ordering [65]. In fact, entering into multiple CDW $\boldsymbol{q}$-vectors regime on reduction of Sb content below $x < 0.29$, a clear magnetic transition featuring a drop in $\chi_{\perp}$ below $T_N \approx 2.01$ K for $x = 0.10$ and $T_N \approx 2.04$ K for $x = 0$ ($NdTe_2$) is observed. For $\chi_{//}$, the magnetic transitions in both samples manifest into weak features as shown in the insets in Fig. 2. This susceptibility behavior is distinct than the stronger susceptibility drop observed below T_N in $\chi_{//}$ for Sb-rich compositions and in both $\chi_{//}$ and $\chi_{\perp}$ for intermediate Sb-compositions. Such susceptibility behavior showing drop in $\chi_{\perp}$ but a weak transition in $\chi_{//}$ below T_N is suggestive of the moment reorientation towards the out-of-plane direction or *c*-axis, consistent with a much larger $M_{\perp}$ than $M_{//}$ in $M(H)$ measurement for $x = 0.10$ and 0 (Fig. 4). In fact, the switching of magnetic anisotropy from in-plane direction in high-Sb compositions $x = 1$ and 0.82 to out-of-plane direction in Sb-less samples $x = 0.10$ and 0 can be directly observed in the $\chi(\theta)$ measurement. As shown in Fig. 3(c), the $\chi(\theta)$ for $x = 0$ exhibits completely opposite trend in comparison to $x = 1$ sample with maximum and minimum value along the out-of-plane and in-plane fields respectively.

These results clearly demonstrate the complex interaction between CDW and magnetism proposed in earlier *Ln*SbTe studies [33,62,65], which can also be understood by the evolution of magnetic parameters such as Curie-Weiss temperature (θ_{cw}) and effective magnetic moment (μ_{eff}) [Fig. 3(b)]. These parameters are extracted by fitting the $\chi(T)$ data in the paramagnetic phase using a modified Curie-Weiss model $\chi_{mol} = \chi_0 + C/(T-\theta_{cw})$, where χ_0 is the temperature independent part of susceptibility and C is Curie constant. From the fitting, we found negative θ_{cw} for all the samples as expected for their AFM ground state. As shown in Fig. 3(b), the θ_{cw} lacks the systematic dependence on Sb content x with significantly different θ_{cw} for two end compounds $x = 0$ ($\theta_{cw} \approx -29.5$ K) and 1 ($\theta_{cw} \approx -7.8$ K), which is distinct than the systematic variation in $CeSb_xTe_{2-x-\delta}$ [62]

and $GdSb_xTe_{2-x-\delta}$ [63]. Higher (more negative) θ_{cw} for $x = 0$ in comparison to $x = 1$ sample implies stronger AFM interaction in $NdTe_2$ ($x = 0$), however its T_N is lower than that of $NdSbTe_{1.08}$ ($x = 1$). Between these two end compounds, the variation of θ_{cw} that gives the information about magnetic exchange interactions is also unable to explain the evolution of T_N with Sb-Te substitution. Such discrepancy between the composition dependence of θ_{cw} and T_N suggests the additional contribution affecting the formation of long-range AFM ordering in $NdSb_xTe_{2-x+\delta}$, which has also been proposed in $GdSb_xTe_{2-x-\delta}$ [63]. Thus, the role of CDW in tuning magnetism seems plausible in this family.

In addition, from the Curie constant we have obtained the effective moments by $\mu_{eff} = \sqrt{\frac{3k_BC}{N_A}}$, where N_A is the Avogadro's number and k_B is the Boltzmann constant. The obtained μ_{eff} also exhibits a non-monotonic dependence on Sb content x with a value of 3.70 μ_B for $NdSbTe_{1.08}$ ($x = 1$) that is slightly different than the theoretically expected value of 3.62 μ_B [shown by a dashed line in Fig. 3(b)] for a Nd^{3+} ion with a $4f^3$ configuration. The μ_{eff} is further deviated from the theoretical value with increasing substitution and becomes minimum for $x = 0.82$ ($\mu_{eff} \approx 2.85\ \mu_B$, which is consistent with tetragonal to orthorhombic phase boundary that activates the CDW. On reducing the Sb content to $x = 0.60$, the μ_{eff} start to approach the theoretical value which is slightly surpassed on further decreasing Sb content to $x = 0.45$ and reaching a maximum $\mu_{eff} \approx 4.05\ \mu_B$ for $x = 0.29$ that appears to align with single to multiple CDW $\boldsymbol{q}$-vectors transition below which μ_{eff} decreases to a value of $\mu_{eff} \approx 3.38\ \mu_B$ for $x = 0$. Such variation of μ_{eff} also indicates the interplay between CDW and magnetism, which is in stark contrast to $CeSb_xTe_{2-x-\delta}$ [62] and $GdSb_xTe_{2-x-\delta}$ [63] where μ_{eff} has been reported to be close to the theoretical values for Ce^{3+} and Gd^{3+} ions respectively over entire Sb-Te composition. The deviation from theoretical μ_{eff} with Sb-Te substitution in

$NdSb_xTe_{2-x+\delta}$ might be attributed to a few reasons such as varying spin-orbit coupling (SOC) [82], crystal electric field effect (CEF) [83] and/or the hybridization between the 4*f* moments and conductions electrons [84–87]. The SOC is less likely to play a significant role given the fact that the Sb-Te substitution in $CeSb_xTe_{2-x-\delta}$ [62] and $GdSb_xTe_{2-x-\delta}$ [63], which would cause a similar variation of SOC, has less effect on μ_{eff}. In addition, the CEF on 4*f* electrons is negligible because they are well-screened by the electrons of 5*s* and 5*p* orbitals [88,89]. This implies that the coupling of 4*f* moments and conductions electrons generated by Sb bands could cause the variation of μ_{eff} from the theoretical value. This further supports the interplay between magnetism and CDW induced by distorted Sb-square net. Such coupling of magnetism and CDW might also be the origin for the reorientation of Nd moments that leads to the change in magnetic structure with Sb-Te substitution in $NdSb_xTe_{2-x+\delta}$, which is again distinct than the similar AFM configuration over an entire composition range in $CeSb_xTe_{2-x-\delta}$ [62] and $GdSb_xTe_{2-x-\delta}$ [33]. Further neutron scattering experiment on a wide range of $NdSb_xTe_{2-x+\delta}$ compositions similar to a recent study on two Nd-based samples $NdSb_{0.94}Te_{0.92}$ and $NdSb_{0.48}Te_{1.37}$ [65] is needed to clarify the interplay between magnetism and CDW as well as the evolution of magnetic structure in $NdSb_xTe_{2-x+\delta}$.

The reorientation of magnetic moments has been proposed to break various symmetries and consequently tune the topological states in AFM TSM [90–92]. For example, in a TSM candidate $YbMnSb_2$ [90], a *C*-type AFM ordering with out-of-plane or canted moments have been predicted to give rise to a gapped Dirac crossing or Weyl nodes, respectively. Similar modulation of topological states depending on moment orientation has also been predicted [91,92] and experimentally verified [91] in another TSM candidate FeSn. Substituting Co for Fe in FeSn reorient AFM moments from in-plane to out-of-plane direction which breaks the nonsymmorphic symmetry leading to a theoretically predicted gap at the Dirac point [91]. In *Ln*SbTe, the

topological band structure can be controlled by Sb-Te substitution, providing access to an ideal Dirac state located near the Fermi level (E_F) for intermediate Sb compositions $CeSb_{0.51}Te_{1.40}$ [62] and $GdSb_{0.46}Te_{1.48}$ [61] where all trivial bands at the E_F are gapped out by CDW. However, as discussed earlier, both $CeSb_xTe_{2-x-\delta}$ [62] and $GdSb_xTe_{2-x-\delta}$ [33] exhibit similar spin orientation for entire Sb composition. Therefore, $NdSb_xTe_{2-x+\delta}$ studied in this work which displays switching of easy axis between in-plane and out-of-plane directions could be an ideal platform to investigate the interplay between moment reorientation and non-trivial band topology.

In addition to symmetry breaking induced by moment reorientation, tuning magnetic states by applying magnetic field has also been proposed to modify the topological phases in CeSbTe [28]. The AFM ground state in CeSbTe is found to exhibit field-driven metamagnetic transition and a subsequent ferromagnetic (FM)-like polarization [28], which provides an approach to switch on/off the time-reversal symmetry and is predicted to tune topological states [28]. Also a field driven moment polarization to FM state has been demonstrated to lead to a topological phase transition from AFM topological insulator to time reversal symmetry-breaking Weyl state in $MnBi_2Te_4$ [93]. Here, as seen in field-dependence of magnetization $M(H)$ measurements at $T = 2$ K for all $NdSb_xTe_{2-x+\delta}$ samples (Fig. 4), the isothermal magnetization becomes sublinear at high field but lacks a clear saturation behavior seen in true ferromagnets and their values at $\mu_0H = 9$ T are smaller than the saturation moment of 3.62 μ_B for a Nd^{3+} ion. Therefore, the high-field sublinear magnetization in $NdSb_xTe_{2-x+\delta}$ might be attributed to a possible new canted AFM state with partial polarization of moments. We calculated the derivative of $M(H)$ data [$dM/d(\mu_0H)$] to precisely determine the field-driven metamagnetic (MM) transition and partial spin polarization (PP), which was used in an earlier NdSbTe study where a sharp peak followed by a broad hump or shoulder at higher field are defined as metamagnetic transition (H_{MM}) and partial spin polarization (H_{PP}) fields,

respectively [65]. The field-dependence of $dM/d(\mu_0 H)$ data under $H//ab$ and $H//c$ fields for samples representing three different AFM regions [AFM_{ab}, cAFM, and AFM_c in Fig. 3(a)] showing H_{MM} and H_{PP} are presented in Fig. 5(a). Based on these results, we constructed a magnetic phase diagram at $T = 2$ K [Fig. 5(b)] which depicts the evolution of magnetic states with Sb content x. First, in AFM_{ab} region, the $x = 1$ sample exhibits AFM to partial moment polarization featuring sublinear magnetization at higher in-plane magnetic field ($H//ab$) while the $x = 0.82$ undergoes AFM to MM transition before partial polarization at $H//ab$ only, consistent with their in-plane moments as discussed earlier. Decreasing Sb content below $x < 0.82$ systematically reduces both H_{MM} and H_{PP} in cAFM region, however these transitions occur under both in-plane and out-of-plane fields that is line with their canted moments. As mentioned above, further reducing Sb content to $x = 0.10$ and 0 switches easy axis towards the out-of-plane direction and thus features transition from AFM to partial spin polarization (without low-field metamagnetic transition) for $H//c$ field only. This demonstrates rich magnetic phases in $NdSb_xTe_{2-x+\delta}$ depending on both Sb composition and applied field, which provides a rare platform to explore coupling between magnetism and electronic band topology.

In conclusion, we have investigated the magnetic properties of $NdSb_xTe_{2-x+\delta}$ over the entire composition range. This work reveals an interesting non-monotonic evolution of T_N accompanied by a systematic reorientation of moments from in-plane to out-of-plane direction with decreasing Sb content x. The rich magnetic phases in $NdSb_xTe_{2-x+\delta}$ provide useful insights for the evolution of magnetism in *Ln*SbTe materials, offering a good platform for tunable topological states.

Acknowledgement

This work was primarily (synthesis and magnetic property up to 9T) supported by the U.S. Department of Energy, Office of Science, Basic Energy Sciences program under Grant No. DE-SC0022006. M. M. and R. B. acknowledge μ-ATOMS, an Energy Frontier Research Center funded by DOE, Office of Science, Basic Energy Sciences, under Award DE-SC0023412 for part of the analysis. J. S. acknowledges the support from NIH under award P20GM103429 for powder XRD. J. W. acknowledges the support from the U.S. National Science Foundation under grand DMR-2316811 for structure refinement. J. H. acknowledges National Science Foundation under grand DMR-1906383 for angular dependent magnetization measurements using MPMS.

References

[1] M. Z. Hasan and C. L. Kane, *Colloquium: Topological Insulators*, Rev. Mod. Phys. **82**, 3045 (2010).

[2] L. Fu, *Topological Crystalline Insulators*, Phys. Rev. Lett. **106**, 106802 (2011).

[3] T. Liang, Q. Gibson, M. N. Ali, M. Liu, R. J. Cava, and N. P. Ong, *Ultrahigh Mobility and Giant Magnetoresistance in the Dirac Semimetal Cd_3As_2*, Nat Mater **14**, 280 (2015).

[4] Q. Li, D. E. Kharzeev, C. Zhang, Y. Huang, I. Pletikosić, A. V. Fedorov, R. D. Zhong, J. A. Schneeloch, G. D. Gu, and T. Valla, *Chiral Magnetic Effect in $ZrTe_5$*, Nature Phys **12**, 6 (2016).

[5] Y.-S. Jho and K.-S. Kim, *Interplay between Interaction and Chiral Anomaly: Anisotropy in the Electrical Resistivity of Interacting Weyl Metals*, Phys. Rev. B **87**, 205133 (2013).

[6] S.-Y. Xu et al., *Observation of Fermi Arc Surface States in a Topological Metal*, Science **347**, 294 (2015).

[7] S.-Y. Xu et al., *Discovery of a Weyl Fermion State with Fermi Arcs in Niobium Arsenide*, Nature Phys **11**, 9 (2015).

[8] B. Q. Lv et al., *Experimental Discovery of Weyl Semimetal TaAs*, Phys. Rev. X **5**, 031013 (2015).

[9] S.-M. Huang et al., *A Weyl Fermion Semimetal with Surface Fermi Arcs in the Transition Metal Monopnictide TaAs Class*, Nat Commun **6**, 1 (2015).

[10] A. Sakai et al., *Giant Anomalous Nernst Effect and Quantum-Critical Scaling in a Ferromagnetic Semimetal*, Nature Phys **14**, 11 (2018).

[11] S. N. Guin et al., *Anomalous Nernst Effect beyond the Magnetization Scaling Relation in the Ferromagnetic Heusler Compound Co_2MnGa*, NPG Asia Mater **11**, 1 (2019).

[12] K. Manna et al., *From Colossal to Zero: Controlling the Anomalous Hall Effect in Magnetic Heusler Compounds via Berry Curvature Design*, Phys. Rev. X **8**, 041045 (2018).

[13] P. Li et al., *Giant Room Temperature Anomalous Hall Effect and Tunable Topology in a Ferromagnetic Topological Semimetal Co_2MnAl*, Nat Commun **11**, 1 (2020).

[14] E. Vilanova Vidal, G. Stryganyuk, H. Schneider, C. Felser, and G. Jakob, *Exploring Co_2MnAl Heusler Compound for Anomalous Hall Effect Sensors*, Applied Physics Letters **99**, 132509 (2011).

[15] E. Liu et al., *Giant Anomalous Hall Effect in a Ferromagnetic Kagome-Lattice Semimetal*, Nature Phys **14**, 11 (2018).

[16] S. N. Guin et al., *Zero-Field Nernst Effect in a Ferromagnetic Kagome-Lattice Weyl-Semimetal $Co_3Sn_2S_2$*, Advanced Materials **31**, 1806622 (2019).

[17] M. Kang et al., *Dirac Fermions and Flat Bands in the Ideal Kagome Metal FeSn*, Nat Mater **19**, 163 (2020).

[18] L. Ye et al., *Massive Dirac Fermions in a Ferromagnetic Kagome Metal*, Nature **555**, 7698 (2018).

[19] A. Sakai et al., *Iron-Based Binary Ferromagnets for Transverse Thermoelectric Conversion*, Nature **581**, 7806 (2020).

[20] K. Kim et al., *Large Anomalous Hall Current Induced by Topological Nodal Lines in a Ferromagnetic van Der Waals Semimetal*, Nature Mater **17**, 9 (2018).

[21] S. Nakatsuji, N. Kiyohara, and T. Higo, *Large Anomalous Hall Effect in a Non-Collinear Antiferromagnet at Room Temperature*, Nature **527**, 7577 (2015).

[22] M. Ikhlas, T. Tomita, T. Koretsune, M.-T. Suzuki, D. Nishio-Hamane, R. Arita, Y. Otani, and S. Nakatsuji, *Large Anomalous Nernst Effect at Room Temperature in a Chiral Antiferromagnet*, Nature Phys **13**, 11 (2017).

[23] A. K. Nayak et al., *Large Anomalous Hall Effect Driven by a Nonvanishing Berry Curvature in the Noncolinear Antiferromagnet Mn_3Ge*, Science Advances **2**, e1501870 (2016).

[24] C. Wuttke et al., *Berry Curvature Unravelled by the Anomalous Nernst Effect in Mn_3Ge*, Phys. Rev. B **100**, 085111 (2019).

[25] T. Suzuki, R. Chisnell, A. Devarakonda, Y.-T. Liu, W. Feng, D. Xiao, J. W. Lynn, and J. G. Checkelsky, *Large Anomalous Hall Effect in a Half-Heusler Antiferromagnet*, Nature Phys **12**, 12 (2016).

[26] A. A. Burkov, *Anomalous Hall Effect in Weyl Metals*, Phys. Rev. Lett. **113**, 187202 (2014).

[27] J. Noky, Y. Zhang, J. Gooth, C. Felser, and Y. Sun, *Giant Anomalous Hall and Nernst Effect in Magnetic Cubic Heusler Compounds*, Npj Comput Mater **6**, 1 (2020).

[28] L. M. Schoop et al., *Tunable Weyl and Dirac States in the Nonsymmorphic Compound CeSbTe*, Science Advances (2018).

[29] B. Lv, J. Chen, L. Qiao, J. Ma, X. Yang, M. Li, M. Wang, Q. Tao, and Z.-A. Xu, *Magnetic and Transport Properties of Low-Carrier-Density Kondo Semimetal CeSbTe*, J. Phys.: Condens. Matter **31**, 355601 (2019).

[30] R. Singha, T. H. Salters, S. M. L. Teicher, S. Lei, J. F. Khoury, N. P. Ong, and L. M. Schoop, *Evolving Devil's Staircase Magnetization from Tunable Charge Density Waves in Nonsymmorphic Dirac Semimetals*, Advanced Materials **33**, 2103476 (2021).

[31] M. M. Hosen et al., *Discovery of Topological Nodal-Line Fermionic Phase in a Magnetic Material GdSbTe*, Sci Rep **8**, 13283 (2018).

[32] R. Sankar et al., *Crystal Growth and Magnetic Properties of Topological Nodal-Line Semimetal GdSbTe with Antiferromagnetic Spin Ordering*, Inorg. Chem. **58**, 11730 (2019).

[33] S. Lei, A. Saltzman, and L. M. Schoop, *Complex Magnetic Phases Enriched by Charge Density Waves in the Topological Semimetals* $GdSb_xTe_{2-x-\delta}$, Phys. Rev. B **103**, 134418 (2021).

[34] S. Lei, V. Duppel, J. M. Lippmann, J. Nuss, B. V. Lotsch, and L. M. Schoop, *Charge Density Waves and Magnetism in Topological Semimetal Candidates* $GdSb_xTe_{2-x-\delta}$, Advanced Quantum Technologies **2**, 1900045 (2019).

[35] K. Pandey et al., *Magnetic Topological Semimetal Phase with Electronic Correlation Enhancement in SmSbTe*, Advanced Quantum Technologies **4**, 2100063 (2021).

[36] K. Pandey, R. Basnet, J. Wang, B. Da, and J. Hu, *Evolution of Electronic and Magnetic Properties in the Topological Semimetal* $SmSb_xTe_{2-x}$, Phys. Rev. B **105**, 155139 (2022).

[37] K. Pandey, R. Basnet, A. Wegner, G. Acharya, M. R. U. Nabi, J. Liu, J. Wang, Y. K. Takahashi, B. Da, and J. Hu, *Electronic and Magnetic Properties of the Topological Semimetal Candidate NdSbTe*, Phys. Rev. B **101**, 235161 (2020).

[38] R. Sankar, I. P. Muthuselvam, K. Rajagopal, K. Ramesh Babu, G. S. Murugan, K. S. Bayikadi, K. Moovendaran, C. Ting Wu, and G.-Y. Guo, *Anisotropic Magnetic Properties of Nonsymmorphic Semimetallic Single Crystal NdSbTe*, Crystal Growth & Design **20**, 6585 (2020).

[39] M. Yang, Y. Qian, D. Yan, Y. Li, Y. Song, Z. Wang, C. Yi, H. L. Feng, H. Weng, and Y. Shi, *Magnetic and Electronic Properties of a Topological Nodal Line Semimetal Candidate: HoSbTe*, Phys. Rev. Materials **4**, 094203 (2020).

[40] S. Yue et al., *Topological Electronic Structure in the Antiferromagnet HoSbTe*, Phys. Rev. B **102**, 155109 (2020).

[41] F. Gao, J. Huang, W. Ren, M. Li, H. Wang, T. Yang, B. Li, and Z. Zhang, *Magnetic and Transport Properties of the Topological Compound DySbTe*, Phys. Rev. B **105**, 214434 (2022).

[42] F. Gao et al., *Magnetic and Magnetotransport Properties of the Magnetic Topological Nodal-Line Semimetal TbSbTe*, Advanced Quantum Technologies **6**, 2200163 (2023).

[43] I. Plokhikh, V. Pomjakushin, D. J. Gawryluk, O. Zaharko, and E. Pomjakushina, *Competing Magnetic Phases in LnSbTe (Ln = Ho and Tb)*, Inorg. Chem. **61**, 11399 (2022).

[44] I. Plokhikh, V. Pomjakushin, D. Jakub Gawryluk, O. Zaharko, and E. Pomjakushina, *On the Magnetic Structures of 1:1:1 Stoichiometric Topological Phases LnSbTe (Ln = Pr, Nd, Dy and Er)*, Journal of Magnetism and Magnetic Materials **583**, 171009 (2023).

[45] Q. Xu, Z. Song, S. Nie, H. Weng, Z. Fang, and X. Dai, *Two-Dimensional Oxide Topological Insulator with Iron-Pnictide Superconductor LiFeAs Structure*, Phys. Rev. B **92**, 205310 (2015).

[46] L. M. Schoop, M. N. Ali, C. Straßer, A. Topp, A. Varykhalov, D. Marchenko, V. Duppel, S. S. P. Parkin, B. V. Lotsch, and C. R. Ast, *Dirac Cone Protected by Non-Symmorphic Symmetry and Three-Dimensional Dirac Line Node in ZrSiS*, Nat Commun **7**, 11696 (2016).

[47] J. Hu et al., *Evidence of Topological Nodal-Line Fermions in ZrSiSe and ZrSiTe*, Phys. Rev. Lett. **117**, 016602 (2016).

[48] R. Lou et al., *Emergence of Topological Bands on the Surface of ZrSnTe Crystal*, Phys. Rev. B **93**, 241104 (2016).

[49] M. Neupane et al., *Observation of Topological Nodal Fermion Semimetal Phase in ZrSiS*, Phys. Rev. B **93**, 201104 (2016).

[50] D. Takane, Z. Wang, S. Souma, K. Nakayama, C. X. Trang, T. Sato, T. Takahashi, and Y. Ando, *Dirac-Node Arc in the Topological Line-Node Semimetal HfSiS*, Phys. Rev. B **94**, 121108 (2016).

[51] M. M. Hosen et al., *Tunability of the Topological Nodal-Line Semimetal Phase in ZrSiX-Type Materials (X= S, Se, Te)*, Phys. Rev. B **95**, 161101 (2017).

[52] C. Chen et al., *Dirac Line Nodes and Effect of Spin-Orbit Coupling in the Nonsymmorphic Critical Semimetals MSiS (M=Hf, Zr)*, Phys. Rev. B **95**, 125126 (2017).

[53] B.-B. Fu et al., *Dirac Nodal Surfaces and Nodal Lines in ZrSiS*, Sci Adv **5**, eaau6459 (2019).

[54] A. Topp, J. M. Lippmann, A. Varykhalov, V. Duppel, B. V. Lotsch, C. R. Ast, and L. M. Schoop, *Non-Symmorphic Band Degeneracy at the Fermi Level in ZrSiTe*, New J. Phys. **18**, 125014 (2016).

[55] S. Pezzini, M. R. van Delft, L. M. Schoop, B. V. Lotsch, A. Carrington, M. I. Katsnelson, N. E. Hussey, and S. Wiedmann, *Unconventional Mass Enhancement around the Dirac Nodal Loop in ZrSiS*, Nat. Phys. **14**, 178 (2018).

[56] Y. Shao et al., *Electronic Correlations in Nodal-Line Semimetals*, Nat. Phys. **16**, 636 (2020).

[57] S. Regmi, R. Smith, A. P. Sakhya, M. Sprague, M. I. Mondal, I. B. Elius, N. Valadez, A. Ptok, D. Kaczorowski, and M. Neupane, *Observation of Gapless Nodal-Line States in NdSbTe*, Phys. Rev. Mater. **7**, 044202 (2023).

[58] S. Regmi, G. Dhakal, F. C. Kabeer, N. Harrison, F. Kabir, A. P. Sakhya, K. Gofryk, D. Kaczorowski, P. M. Oppeneer, and M. Neupane, *Observation of Multiple Nodal Lines in SmSbTe*, Phys. Rev. Mater. **6**, L031201 (2022).

[59] K. Pandey, L. Sayler, R. Basnet, J. Sakon, F. Wang, and J. Hu, *Crystal Growth and Electronic Properties of LaSbSe*, Crystals **12**, 11 (2022).

[60] S. Acharya, K. Pandey, R. Basnet, G. Acharya, M. R. U. Nabi, J. Wang, and J. Hu, *Single Crystal Growth and Characterization of Topological Semimetal ZrSnTe*, Journal of Alloys and Compounds **968**, 171903 (2023).

[61] S. Lei et al., *Band Engineering of Dirac Semimetals Using Charge Density Waves*, Advanced Materials **33**, 2101591 (2021).

[62] R. Singha, T. H. Salters, S. M. L. Teicher, S. Lei, J. F. Khoury, N. P. Ong, and L. M. Schoop, *Evolving Devil's Staircase Magnetization from Tunable Charge Density Waves in Nonsymmorphic Dirac Semimetals*, Advanced Materials **33**, 2103476 (2021).

[63] S. Lei, V. Duppel, J. M. Lippmann, J. Nuss, B. V. Lotsch, and L. M. Schoop, *Charge Density Waves and Magnetism in Topological Semimetal Candidates $GdSb_xTe_{2-x-\delta}$*, Advanced Quantum Technologies **2**, 1900045 (2019).

[64] P. Li et al., *Charge Density Wave and Weak Kondo Effect in a Dirac Semimetal CeSbTe*, Sci. China Phys. Mech. Astron. **64**, 237412 (2021).

[65] T. H. Salters, F. Orlandi, T. Berry, J. F. Khoury, E. Whittaker, P. Manuel, and L. M. Schoop, *Charge Density Wave-Templated Spin Cycloid in Topological Semimetal $NdSb_xTe_{2-x-\delta}$*, Phys. Rev. Mater. **7**, 044203 (2023).

[66] S. Klemenz, S. Lei, and L. M. Schoop, *Topological Semimetals in Square-Net Materials*, Annual Review of Materials Research **49**, 185 (2019).

[67] J. Hu, Y. Zhu, X. Gui, D. Graf, Z. Tang, W. Xie, and Z. Mao, *Quantum Oscillation Evidence for a Topological Semimetal Phase in ZrSnTe*, Phys. Rev. B **97**, 155101 (2018).

[68] K. Stöwe, *Crystal Structure, Magnetic Properties and Band Gap Measurements of $NdTe_{2-x}$ ($x = 0.11(1)$)*, Zeitschrift Für Kristallographie - Crystalline Materials **216**, 215 (2001).

[69] H. Poddig, P. Gebauer, K. Finzel, K. Stöwe, and T. Doert, *Structural Variations and Bonding Analysis of the Rare-Earth Metal Tellurides $RETe_{1.875\pm\delta}$ (RE = Ce, Pr, Sm, Gd; $0.004 \leq \delta \leq 0.025$)*, Inorg. Chem. **60**, 11231 (2021).

[70] C. J. Müller, U. Schwarz, and T. Doert, *High-Pressure Syntheses of Lanthanide Polysulfides and Polyselenides $LnX_{1.9}$ (Ln = Gd–Tm, X = S, Se)*, Zeitschrift Für Anorganische Und Allgemeine Chemie **638**, 2477 (2012).

[71] S.-M. Park, S.-J. Park, and S.-J. Kim, *The Superstructure of Semiconducting $SmTe_{2-x}$*, Journal of Solid State Chemistry **140**, 300 (1998).

[72] H. Poddig, T. Donath, P. Gebauer, K. Finzel, M. Kohout, Y. Wu, P. Schmidt, and T. Doert, *Rare Earth Metal Polytellurides $RETe_{1.8}$ (RE = Gd, Tb, Dy) – Directed Synthesis, Crystal and Electronic Structures, and Bonding Features*, Zeitschrift Für Anorganische Und Allgemeine Chemie **644**, 1886 (2018).

[73] R. Wang, H. Steinfink, and W. F. Bradley, *The Crystal Structure of Lanthanum Telluride and of Tellurium-Deficient Neodymium Telluride*, Inorg. Chem. **5**, 142 (1966).

[74] K. Stöwe, *Crystal Structure and Magnetic Properties of $CeTe_2$*, Journal of Alloys and Compounds **307**, 101 (2000).

[75] K. Stöwe, *Die Kristallstruktur von $PrTe_2$*, Zeitschrift für anorganische und allgemeine Chemie **626**, 803 (2000).

[76] K. Stöwe, *Crystal Structure and Electronic Band Structure of $LaTe_2$*, Journal of Solid State Chemistry **149**, 155 (2000).

[77] E. Lee, D. H. Kim, J. D. Denlinger, J. Kim, K. Kim, B. I. Min, B. H. Min, Y. S. Kwon, and J.-S. Kang, *Angle-Resolved and Resonant Photoemission Spectroscopy Study of the Fermi Surface Reconstruction in the Charge Density Wave Systems $CeTe_2$ and $PrTe_2$*, Phys. Rev. B **91**, 125137 (2015).

[78] J.-S. Kang et al., *Fermi Surface Reconstruction in $CeTe_2$ Induced by Charge Density Waves Investigated via Angle Resolved Photoemission*, Phys. Rev. B **85**, 085104 (2012).

[79] K. Y. Shin, V. Brouet, N. Ru, Z. X. Shen, and I. R. Fisher, *Electronic Structure and Charge-Density Wave Formation in $LaTe_{1.95}$ and $CeTe_{2.00}$*, Phys. Rev. B **72**, 085132 (2005).

[80] D. R. Garcia, G.-H. Gweon, S. Y. Zhou, J. Graf, C. M. Jozwiak, M. H. Jung, Y. S. Kwon, and A. Lanzara, *Revealing Charge Density Wave Formation in the $LaTe_2$ System by Angle Resolved Photoemission Spectroscopy*, Phys. Rev. Lett. **98**, 166403 (2007).

[81] Y. S. Shin, C. W. Han, B. H. Min, H. J. Lee, C. H. Choi, Y. S. Kim, D. L. Kim, and Y. S. Kwon, *Anisotropic Magnetization in RTe_2 (R: Ce, Pr, Gd and Sm)*, Physica B: Condensed Matter **291**, 225 (2000).

[82] R. J. Birgeneau, *Magnetic Moment Reduction Via the Orbit-Lattice Interaction for Ce^{3+} in Rare-Earth Ethyl Sulfates*, Phys. Rev. Lett. **19**, 160 (1967).

[83] T. Tsuchida, A. Hashimoto, and Y. Nakamura, *Crystal Field Effect on the Magnetic Properties of $Ce_xLa_{1-x}Bi$*, Journal of the Physical Society of Japan **36**, 685 (1974).

[84] A. Galler, S. Ener, F. Maccari, I. Dirba, K. P. Skokov, O. Gutfleisch, S. Biermann, and L. V. Pourovskii, *Intrinsically Weak Magnetic Anisotropy of Cerium in Potential Hard-Magnetic Intermetallics*, Npj Quantum Mater. **6**, 1 (2021).

[85] L. L. Hirst, *Theory of the Coupling between Conduction Electrons and Moments of 3d and 4f Ions in Metals*, Advances in Physics **27**, 231 (1978).

[86] L. Pourovskii, V. Vildosola, S. Biermann, and A. Georges, *Local Moment vs. Kondo Behavior of the 4f-Electrons in Rare-Earth Iron Oxypnictides*, EPL **84**, 37006 (2008).

[87] M. Nicklas, S. Kirchner, R. Borth, R. Gumeniuk, W. Schnelle, H. Rosner, H. Borrmann, A. Leithe-Jasper, Yu. Grin, and F. Steglich, *Charge-Doping-Driven Evolution of Magnetism and Non-*

Fermi-Liquid Behavior in the Filled Skutterudite $CePt_4Ge_{12-x}Sb_x$, Phys. Rev. Lett. **109**, 236405 (2012).

[88] R. Skomski and D. J. Sellmyer, *Anisotropy of Rare-Earth Magnets*, Journal of Rare Earths **27**, 675 (2009).

[89] E. Sarantopoulou, S. Kobe, Z. Kollia, B. Podmiljšak, P. J. McGuiness, G. Dražić, and A. C. Cefalas, *Magnetic and Optical Properties of Single $4f^n$ and Mixed $4f^{n-1}5d$ Electronic Configurations of Trivalent Rare Earth Ions in Wide Band Gap Dielectric Crystals*, Journal of Magnetism and Magnetic Materials **267**, 182 (2003).

[90] J.-R. Soh, S. M. Tobin, H. Su, I. Zivkovic, B. Ouladdiaf, A. Stunault, J. A. Rodríguez-Velamazán, K. Beauvois, Y. Guo, and A. T. Boothroyd, *Magnetic Structure of the Topological Semimetal $YbMnSb_2$*, Phys. Rev. B **104**, L161103 (2021).

[91] R. G. Moore et al., *Topological Electronic Structure Evolution with Symmetry-Breaking Spin Reorientation in $Fe_{1-x}Co_xSn$*, Phys. Rev. B **106**, 115141 (2022).

[92] Z. Lin et al., *Dirac Fermions in Antiferromagnetic FeSn Kagome Lattices with Combined Space Inversion and Time-Reversal Symmetry*, Phys. Rev. B **102**, 155103 (2020).

[93] S. H. Lee et al., *Evidence for a Magnetic-Field-Induced Ideal Type-II Weyl State in Antiferromagnetic Topological Insulator $Mn(Bi_{1-x}Sb_x)_2Te_4$*, Phys. Rev. X **11**, 031032 (2021).

Table I: Elemental compositions used in the source materials and final compositions in the grown crystals determined by EDS.

Source materials			EDS composition	$NdSb_xTe_{2-x+\delta}$	
Nd	Sb	Te		x	δ
1	0	2	$NdTe_2$	0	0
1	1.2	1	$NdSb_{0.10}Te_{1.93}$	0.10	0.03
1	0.5	1.5	$NdSb_{0.29}Te_{1.73}$	0.29	0.02
1	0.2	0.8	$NdSb_{0.45}Te_{1.57}$	0.45	0.02
1	1.1	0.9	$NdSb_{0.60}Te_{1.48}$	0.60	0.08
1	0.3	0.7	$NdSb_{0.82}Te_{1.22}$	0.82	0.04
1	1.2	0.8	$NdSb_1Te_{1.08}$	1	0.08

Figure 1

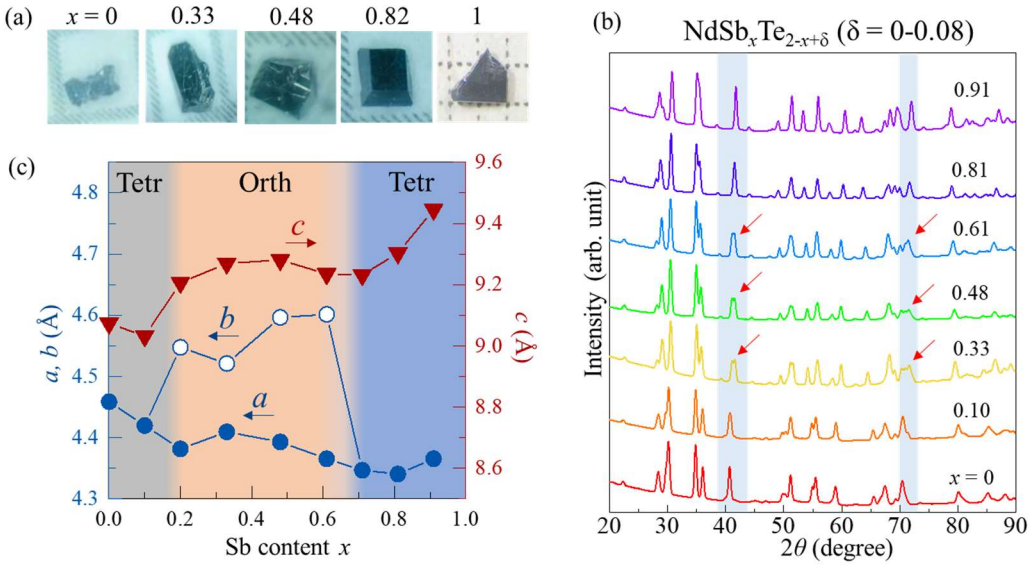

FIG. 1. (a) Optical microscope images of $NdSb_xTe_{2-x+\delta}$ ($0 \leq x \leq 1$) crystals. (b) X-ray diffraction result for $NdSb_xTe_{2-x+\delta}$. (c) Evolution of lattice parameters a, b (Left vertical axis) , and c (Right vertical axis) with varying Sb content x. The Blue, orange, and grey regions represent tetragonal (Tetr), orthorhombic (Orth), and tetragonal (Tetr) lattices, respectively.

Figure 2

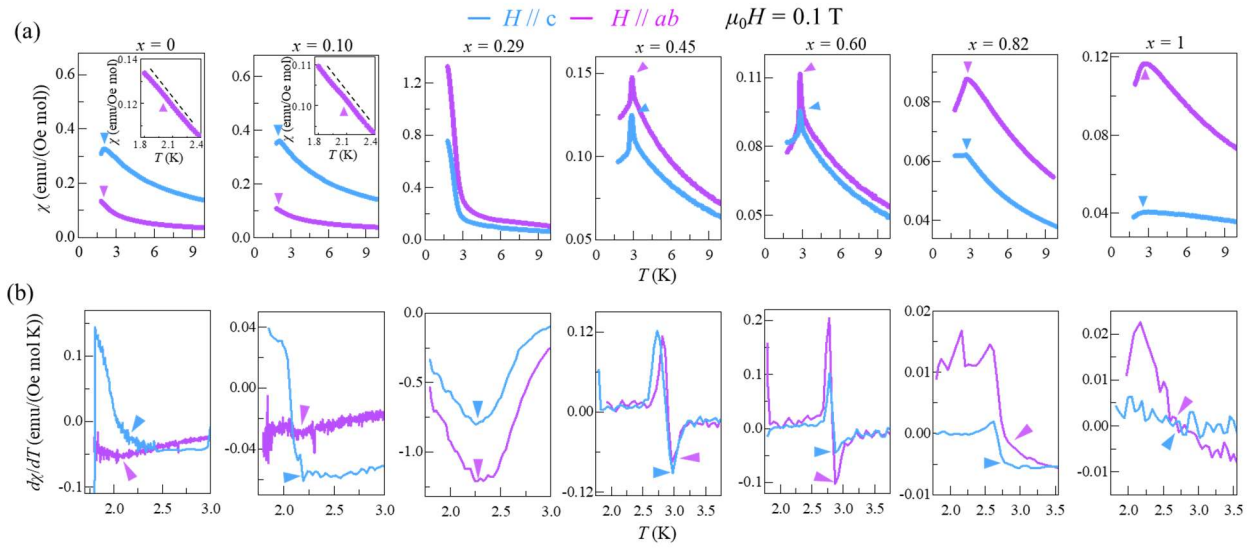

FIG. 2. Temperature dependence of susceptibility for $NdSb_xTe_{2-x+\delta}$ samples under in-plane ($H||ab$, magenta) and out-of-plane ($H//c$, blue) magnetic fields of μ_0H = 0.1 T. Inset: Low-temperature susceptibility under in-plane $H||ab$ field to show magnetic transition clearly. The dashed lines are guide to eye. (b) Temperature dependence of derivative $d\chi/dT$ of $NdSb_xTe_{2-x+\delta}$ samples. The solid triangles denote T_N.

Figure 3

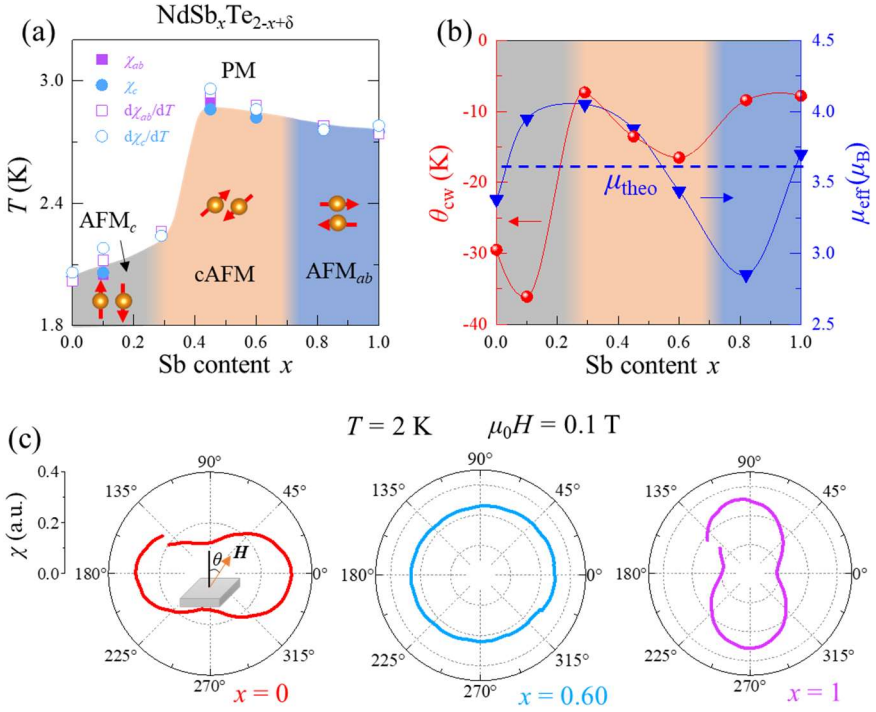

FIG. 3. (a) Evolution of T_N with varying Sb content x. Different colored regions denote distinct orientations for Nd moments. The in-plane, canted, and out-of-plane antiferromagnetic configurations are denoted as AFM$_{ab}$, cAFM, and AFM$_c$ whereas PM represents a paramagnetic state. The moment orientations in each phase region are schematic to show the magnetic easy axis. Here, χ_{ab} and χ_c represent the susceptibility along the ab-plane and c-axis, respectively. (b) Evolution of effective magnetic moment μ_{eff} and Curie-Weiss temperature θ_{CW} with varying Sb content x. The dashed line represents the theoretical μ_{eff}. (c) Angular dependence of susceptibility for x = 0, 0.60, and 1 sample under magnetic fields of μ_0H = 0.1 T and T = 2 K.

Figure 4

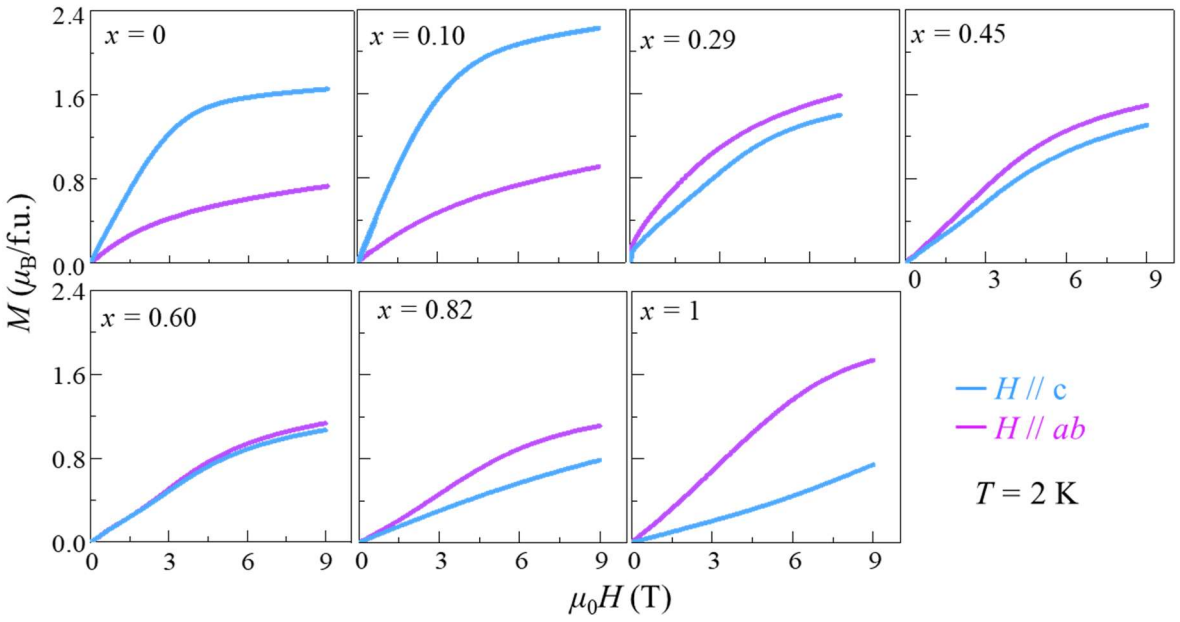

FIG. 4. Field dependence of magnetization for $NdSb_xTe_{2-x+\delta}$ samples under in-plane ($H||ab$, magenta) and out-of-plane ($H//c$, blue) magnetic fields at $T = 2$ K.

Figure 5

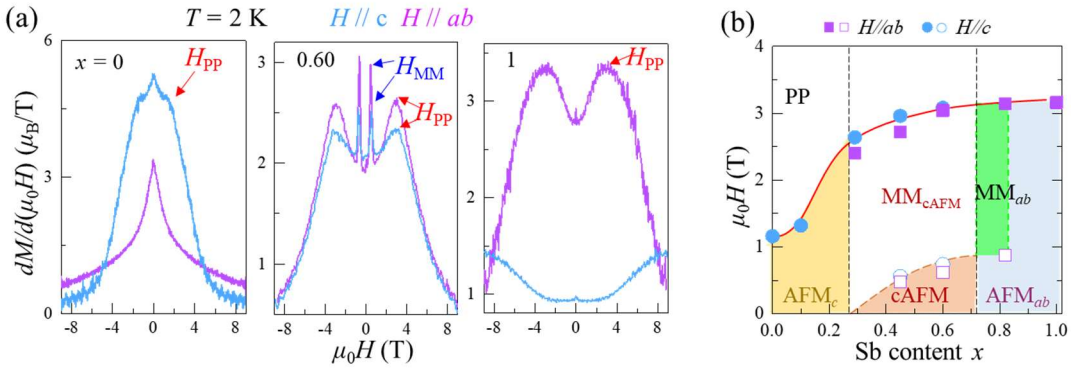

FIG. 5. (a) Field dependence of derivative $dM/d(\mu_0 H)$ under in-plane ($H||ab$, magenta) and out-of-plane ($H//c$, blue) magnetic fields at $T = 2$ K. The metamagnetic and partial spin polarization fields are represented as H_{MM} (Blue color) and H_{PP} (Red color), respectively. (b) Magnetic phase diagram constructed from the field dependence of magnetization measurements presented in Fig. 3. The in-plane, canted, and out-of-plane antiferromagnetic configurations are denoted as AFM_{ab}, cAFM, and AFM_c. The metamagnetic transition for in-plane and canted antiferromagnetic states are represented as MM_{ab} and MM_{cAFM}, respectively. The partial spin polarization is denoted as PP.